Eclipsing the X-Ray Emitting Region in the Active Galaxy NGC 6814

Luigi C. Gallo[1], Adam G. Gonzalez[1] [iD], and Jon M. Miller[2]
[1] Department of Astronomy & Physics, Saint Mary's University, 923 Robie Street, Halifax, NS B3H 3C3, Canada; luigi.gallo@smu.ca
[2] Department of Astronomy, The University of Michigan, 1085 South University Avenue, Ann Arbor, MI 48103, USA

Abstract

We report the detection of a rapid occultation event in the nearby Seyfert galaxy NGC 6814, simultaneously captured in a transient light curve and spectral variability. The intensity and hardness ratio curves capture distinct ingress and egress periods that are symmetric in duration. Independent of the selected continuum model, the changes can be simply described by varying the fraction of the central engine that is covered by transiting obscuring gas. Together, the spectral and timing analyses self-consistently reveal the properties of the obscuring gas, its location to be in the broad-line region, and the size of the X-ray source to be $\sim 25\, r_g$. Our results demonstrate that obscuration close to massive black holes can shape their appearance, and can be harnessed to measure the active region that surrounds the event horizon.

1. Introduction

The innermost region around an accreting supermassive black hole produces the bulk of the radiation that defines active galactic nuclei (AGN). This central engine is unresolved with current detectors, but simple calculations predict a light travel time of minutes to hours across the compact region.

The very hot gas in this region produces X-rays, which can be used to measure the extreme relativistic effects and size scales close to the black hole (Fabian et al. 2009; Wilkins & Gallo 2015; Chainakun & Young 2017; Chartas et al. 2017; Wilkins et al. 2017; Alston et al. 2020). X-ray eclipses of this region are then particularly incisive, because they can deliver clear constraints on size scales in the absence of imaging (Risaliti et al. 2007, 2009, 2011; Kaastra et al. 2018; Turner et al. 2018; Zoghbi et al. 2019; Reichert et al. 1986). When size scales are known, the radiation processes that power the AGN and the nature of the inner flow are determined.

NGC 6814 ($z = 0.00521$) is a Seyfert 1.5 active galaxy characterized by moderate absorption in its optical and X-ray spectrum (Leighly et al. 1994; Rosenblatt et al. 1994; Walton et al. 2013). The X-rays exhibit rapid variability on short (hours; e.g., Walton et al. 2013) and long (years; e.g., Mukai et al. 2003) timescales. The X-ray spectrum (Walton et al. 2013; Tortosa et al. 2018; Waddell & Gallo 2020) is typical of Seyfert 1.5 AGN (e.g., Waddell & Gallo 2020) possessing weak excesses at low ($\lesssim 1\,\mathrm{keV}$) and high ($\gtrsim 10\,\mathrm{keV}$) energies, and narrow emission in the Fe Kα band.

Here we report the detection of a rapid occultation event, simultaneously captured in a transient light curve and spectral variability. Together, the spectral and timing analyses self-consistently reveal the size of the X-ray source and the properties and location of the obscuring gas (Gallo et al. 2004; Miller et al. 2010; Turner et al. 2017; Mizumoto et al. 2018).

2. Observations and Data Reduction

NGC 6814 was observed for $\sim 131\,\mathrm{ks}$ with XMM-Newton (Jansen et al. 2001) starting 2016 April 8. During the observations the EPIC detectors (Strüder et al. 2001; Turner et al. 2001) were operated in large-window mode and with the medium filter in place. The XMM-Newton Observation Data Files (ODFs) were processed to produce calibrated event lists using the XMM-Newton Science Analysis System (SAS V18.0.0). Light curves were extracted from these event lists to search for periods of high background flaring, which were evident in the final $\sim 15\,\mathrm{ks}$ of the observation. These periods were neglected during analysis rendering a good-time exposure of $\sim 112\,\mathrm{ks}$.

Spectra were extracted from a circular region with a radius of $35''$ centered on the source. The background photons were extracted from an off-source circular region on the same CCD with a radius of $50''$. Pileup was negligible during the observations. Single and double events were selected for the pn detector, and single–quadruple events were selected for the metal-oxide semiconductor (MOS) detectors. EPIC response matrices were generated using the SAS tasks ARFGEN and RMFGEN. The MOS and pn data were compared for consistency and determined to be in agreement within known uncertainties. The reflection grating spectrometer (RGS; den Herder et al. 2001) spectra were extracted using the SAS task RGSPROC and response matrices were generated using RGSRMFGEN. The combined spectra are displayed for presentation purposes.

The spectra were optimally binned (Kaastra & Bleeker 2016) and the backgrounds were modeled. Spectral fitting was performed using XSPEC V12.9.1 (Arnaud 1996) and fit quality is tested using the C-statistic (Cash 1979), since optimal binning allows bins to have a small number of counts (i.e., < 20) and a Gaussian distribution cannot be assumed. All parameters are reported in the rest frame of the source unless specified otherwise, but figures remain in the observed frame. The quoted errors on the model parameters correspond to a 90% confidence level for one interesting parameter. A value for the Galactic column density toward NGC 6814 of $1.53 \times 10^{21}\,\mathrm{cm}^{-2}$ (Willingale et al. 2013) is adopted in all of the spectral fits with appropriate abundances (Wilms et al. 2000).
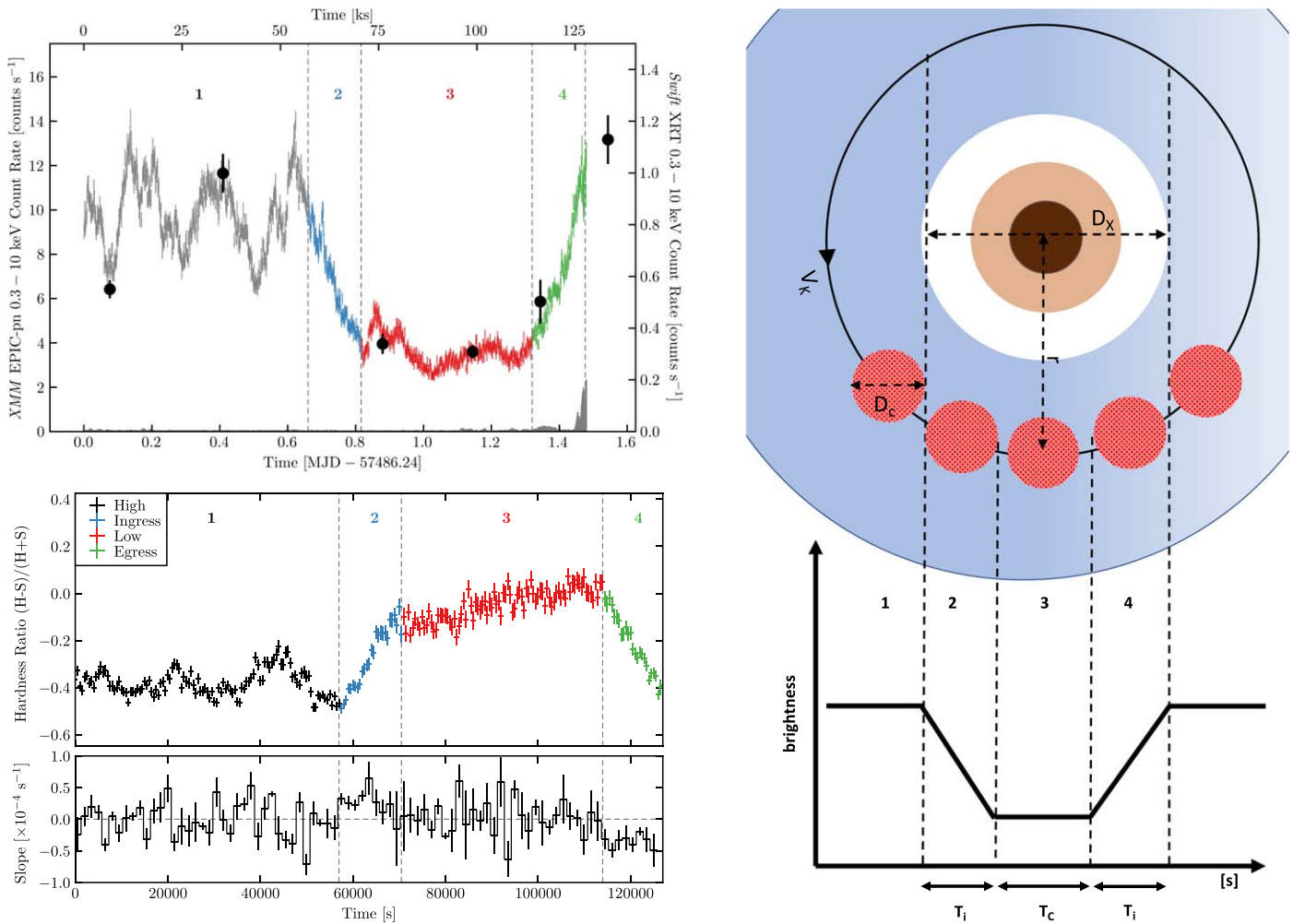
Figure 1. The light curve and hardness ratio curve demonstrating the eclipsing event in NGC 6814. Upper left: the XMM-Newton and Swift (filled circles) 0.3–10 keV light curves of NGC 6814. Prior to ∼55 ks demonstrates the typical random fluctuations in AGN intensity curves. After that time, the light curve shows a constant dimming for ∼13.5 ks, followed by a relatively constant segment for ∼43.5 ks, and then brightening to its original level in ∼13.5 ks. Lower left: with the HR curve in 500 s bins (top panel) we calculate the slope of three neighboring data points before moving over one point and repeating the process until completed for the entire curve, binning the results in 1.5 ks bins (bottom panel). Segments 1 and 3 show random changes in the slope. Segments 2 and 4 mark regions that are defined by progressive hardening and softening, respectively. We take these segments to represent ingress and egress. Right: together the curves are consistent with a transient eclipsing event for which the speculative geometry is shown (the observer is viewing from the bottom of the page).

3. Estimating the Duration of the Eclipse

The 0.3–10 keV light curve is shown in Figure 1. In the first ∼60 ks the object exhibits the flickering behavior that is common in AGN (Vaughan et al. 2003). The light curve then depicts a steady drop in intensity followed by a relatively constant low-flux segment, ending with a steady rise to the predip brightness. This latter part of the light curve is commensurate of the transient brightness curves seen in exoplanet systems made famous with Kepler (Borucki et al. 2010; Steffen et al. 2010).

Determining the start and end time of ingress and egress can be rather arbitrary based on the light curve alone. The hardness ratio (HR) curve is used to estimate these time bins more robustly. With the HR curve in 500 s bins we calculate the slope over three neighboring data points before moving over

one point and repeating the process until completed for the entire curve. The results are then binned in 1.5 ks bins (Figure 1). In this manner, we can determine at what time the slope fluctuations are no longer random. As evident in Figure 1, the HR fluctuations are random in Segments 1 and 3, but consistently hardening in Segment 2 (ingress) and softening in Segment 4 (egress). This method is completely analytical rather than relying on a by-eye approximation.

The ingress and egress in the NGC 6814 light curve are remarkably similar in duration and depth, and the transitions last for approximately $T_i \sim 13.5$ ks. During the minimum, which lasts approximately $T_C \sim 43.5$ ks, the source remains relatively hard and the brightness variations are consistent with the broadband flickering that was evident prior to ingress.

4. Spectral Analysis of the XMM-Newton Data

4.1. Spectral Analysis of the RGS Data

The RGS spectra are examined to determine the influence of the warm absorbers known to exist in this system (Turner et al. 1992; Leighly et al. 1994). Spectra are created during the

Table 1
The RGS Data Fitted with a Double Warm Absorber and a Phenomenological Continuum of a Blackbody and Power Law

Model Component	Model Parameter	Parameter Value
xabs₁	$\log \xi / \mathrm{erg\ cm}^{-2}\ \mathrm{s}^{-1}$	$2.89^{+0.11}_{-0.12}$
	$N_\mathrm{H}/10^{21}\ \mathrm{cm}^{-2}$	$36.8^{+16.7}_{-15.5}$
	$v_\mathrm{out}/\mathrm{km\ s}^{-1}$	5333^{+262}_{-380}
xabs₂	$\log \xi / \mathrm{erg\ cm}^{-2}\ \mathrm{s}^{-1}$	$0.96^{+0.10}_{-0.07}$
	$N_\mathrm{H}/10^{21}\ \mathrm{cm}^{-2}$	3.85 ± 0.72
	$v_\mathrm{out}/\mathrm{km\ s}^{-1}$	5569^{+245}_{-224}
bb	$kT_\mathrm{e}/\mathrm{eV}$	111 ± 5
	$\mathrm{Norm}/10^{-4}$	2.4 ± 0.3
po	Γ	1.5 ± 0.2
	$\mathrm{Norm}/10^{-3}$	7 ± 1
const	$F_\mathrm{low}/F_\mathrm{high}$	0.276 ± 0.009

Note. In XSPEC terminology: tbabs×WA1×WA2 × (bb+po).

high- and low-flux periods, and the two flux-resolved spectra were fitted together between 0.45 and 1.85 keV. Fitting the spectra with a power law plus blackbody to determine the continuum shape and allowing for just a change in the constant of normalization described the general shape of the spectra relatively well, but left several narrow residuals. The fit statistic was $C = 1357$ for 776 dof. A warm absorber was then applied via the XSPEC implementation (Parker et al. 2019) of the SPEX (Kaastra et al. 1996) model XABS (Steenbrugge et al. 2003).

The addition of one warm absorber with free column density (N_H), ionization parameter ($\xi = L/nr^2$, where n is the density of the cloud at a distance r from the source of ionizing luminosity L), and redshift changed the statistic by $\Delta C = 240$ for three additional parameters. The residuals were improved, but significant absorption-like residuals remained around 0.75 keV and 0.95 keV. The addition of a second warm absorber produced a good quality fit without any substantial deviations in the residuals. The final fit to the flux-resolved spectra is $C = 1031$ for 770 dof. The model parameters are shown in Table 1 and the fit residuals are shown in Figure 2. These warm absorbers were applied to the EPIC model for the broadband spectrum.

The low-flux spectrum displays several excess deviations from the described model, exhibiting emission lines not present in the high-flux data. A search for significant positive residuals (i.e., stepping a Gaussian through 0.45–1.85 keV every 5 eV) results in five possible features (Figure 2) at 0.50, 0.57, 0.65, 0.94, and 1.445 keV, with each line improving the fit by $\Delta C > 10$ for three additional free parameters.

4.2. The EPIC-pn Spectra

EPIC-pn spectra were created in each of the four time segments representing the pre-eclipse, ingress, low state, and egress (Figures 3 and 4). The spectra corroborate the behavior in the hardness ratio and light curves. The fractional variability spectrum (F_var; Figure 3), which illustrates the level of variability in each energy band (Edelson et al. 2002), confirms the variations during ingress and egress are predominately at lower energies, and more achromatic during the minimum and pre-ingress periods. Moreover, the variability above $\sim$6 keV is comparable during the entire observation (Figure 3).
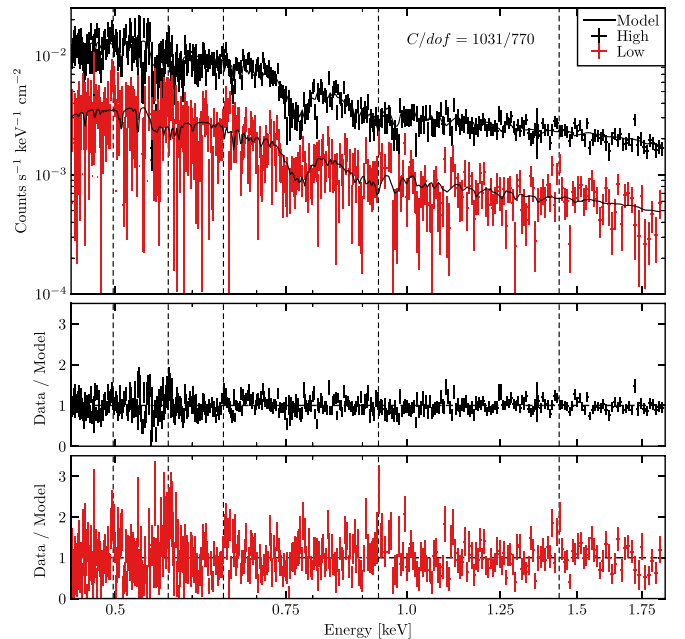

Figure 2. The high-resolution RGS spectra show the presence of a warm absorber and possible emission lines during the low-flux interval. The top panel shows the RGS spectra in the pre-eclipse high-flux state (Segment 1) and the deep minimum flux state (Segment 3). Fitted to the data is a model including two warm absorbers (Table 1) and the residuals (data/model) are shown in the next two panels. The low-flux level can be well described by simply renormalizing the high-flux model. However possible emission-like residuals are evident in the low-flux state (lower panel) at $\sim$0.50, 0.57, 0.65, 0.94, and 1.445 keV, with each line improving the fit by $\Delta C > 10$ for three additional free parameters.

For the simplest model, we fitted the spectra with a single power law plus fixed warm absorbers, modified by a partial coverer. Even with the power law and partial coverer components permitted to vary, this resulted in a relatively poor fit ($C = 2008$ for 728 dof), and demonstrated the need for more physical continuum models. Notwithstanding this, it was notable that the effects of the partial coverer was more enhanced in the low state than during pre-eclipse.

The continuum was modeled assuming the blurred reflection scenario (Ross & Fabian 2005). Here, some fraction of the corona illuminates the inner accretion disk producing back-scattered emission that is modified for Doppler, Special, and General relativistic effects. We use RELXILLD (García et al. 2016; Jiang et al. 2019) to model the scenario, which allows the density of the disk to be altered.

The spectra are modified by the double warm absorber system that was found in the RGS analysis (Figure 2). We determined that refitting the warm absorbers to the pn data did not provide a substantially better fit than simply using the RGS measured parameters. Therefore, the warm absorber parameters were fixed to the RGS values throughout the analysis. An Fe Kα emission line was present in the data, but at energies slightly higher than 6.4 keV. A simple Gaussian profile is used to model this component. The line energy and width were linked between the epochs, but the normalization was left free to examine for variability.

Attempting to fit all four spectra in a self-consistent manner, we allow only the photon index and power-law flux to vary between epochs, which are expected to vary on such timescales. The reflection fraction ($\mathcal{R}$) was linked indicating that the ratio of reflected-to-continuum flux was not changing. This could be
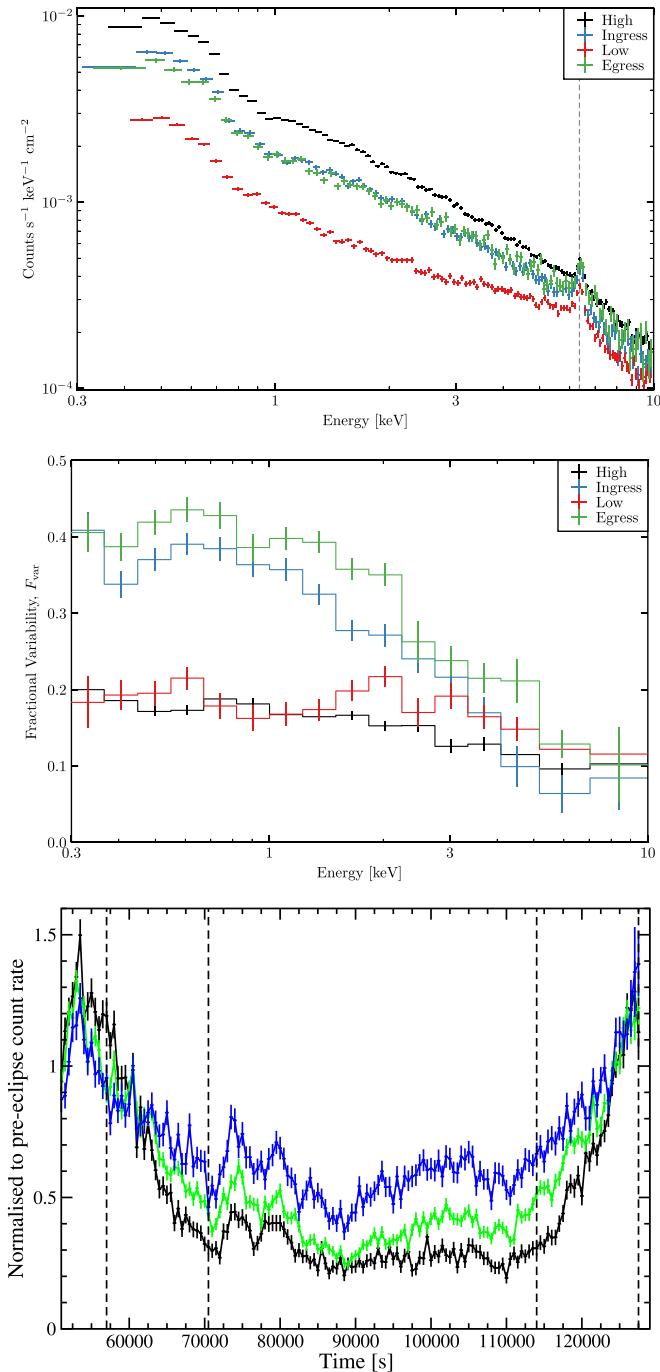
Figure 3. The spectral changes show the effects of the transient absorber and energy dependence on the eclipse. Top: the EPIC-pn spectra are created in the four time segments shown in Figure 1. The spectra are remarkably similar during ingress and egress, and clearly harder when the source is dimmer. Middle: the fractional variability spectra show the degree of variability during the different segments. During ingress and egress, the variability is clearly dominated by the low-energy emission, which would be consistent with increasing absorption. During the high- and low-flux states, the variability is similar suggesting that the nature of the fluctuations are probably alike in the high- and low-flux intervals (i.e., the intrinsic nature has not changed). Above ~ 5 keV, the variability is similar at all flux levels indicating the eclipse has little effect at these highest energies. Bottom: light curves in 0.6–0.8 keV (black), 2–4 keV (green), and 4–6 keV (blue) show the depth of the eclipse is energy dependent as would be expected because of the column density of the cloud. There is indication the shape of the transient may also differ as a function of energy (e.g., see the transitions in the ingress segment).

examined in future modeling, but the rather constant F_{var} spectra (Figure 3) suggests modest spectral variability during the high- and low-flux intervals. This model resulted in a rather poor fit to the data with $C = 2198$ for 737 dof.

A partial coverer was applied to the central X-ray emission component only (i.e., RELXILLD). This was a marked improvement to the fit. The best fit was obtained when the partial coverer had a fixed column density and ionization parameter, but the covering fraction (C_f) was permitted to vary between epochs (Figure 4 and Table 2). In this manner, the covering fraction changed from $C_f \approx 0$ prior to the eclipse and $C_f \approx 0.56$ in the minimum flux state. The final fit statistic was $C = 1029$ for 731 dof.

Allowing the partial coverer to be neutral rather than ionized resulted in a poorer fit ($\Delta C = 22$ for one fewer parameter). Allowing the column density to vary between epochs rather than the covering fraction also resulted in a poorer fit ($C = 1537$ for 731 dof).

We considered if the partial covering results could be dependent on the assumed X-ray continuum. To test this we replaced the blurred reflection model with a soft-Comptonization model for the continuum. This is another commonly used X-ray model that attributes the soft-excess emission to an optically thick warm corona that is situated over the disk (Magdziarz et al. 1998; Czerny et al. 2003; Ballantyne 2020). We adopt the model previously used in Petrucci et al. (2018), which incorporates two NTHCOMP components, one for the traditional optically thin, hot corona and the other for the warm corona. As with the blurred reflection model, the continuum is modified by warm absorbers and a ~ 6.45 keV Gaussian profile is included. Various combinations could be attempted to describe the intrinsic variability. We found the simplest scenario was to link the warm corona parameters, but allow the hot corona to vary from segment to segment.

A partial coverer is again added and the covering fraction is free to vary (Figure 4 and Table 2). The partial coverer column density and ionization parameter are very similar to what was found with the blurred reflection continuum. The covering fractions were offset by about +20% at each interval compared to the reflection model, but the relative change between intervals was the same as in the reflection model. Despite using a different continuum model, the partial covering parameters were very similar. The best-fit soft-Comptonization model resulted in a fit statistic of $C = 1131$ for 728 dof.

5. Discussion and Conclusions

Similar to exoplanet light curves, the transient light curve in NGC 6814 can be interpreted as an occultation event, in this case, of the primary X-ray source by an orbiting globule. Such events have been reported previously (Risaliti et al. 2007, 2011; Turner et al. 2018), but this may be the first time a rapid occultation is captured in its entirety with spectral and temporal data. The symmetry in the transient light curve indicates the obscurer is rather uniform and possibly a single cloud. The rapid timescales of the eclipse place the cloud close to the black hole, and the fact the dip does not reach zero brightness implies the obscurer only partially covers the X-ray source.

The illustration in Figure 1 highlights the situation and demonstrates the parameters that can be estimated from the
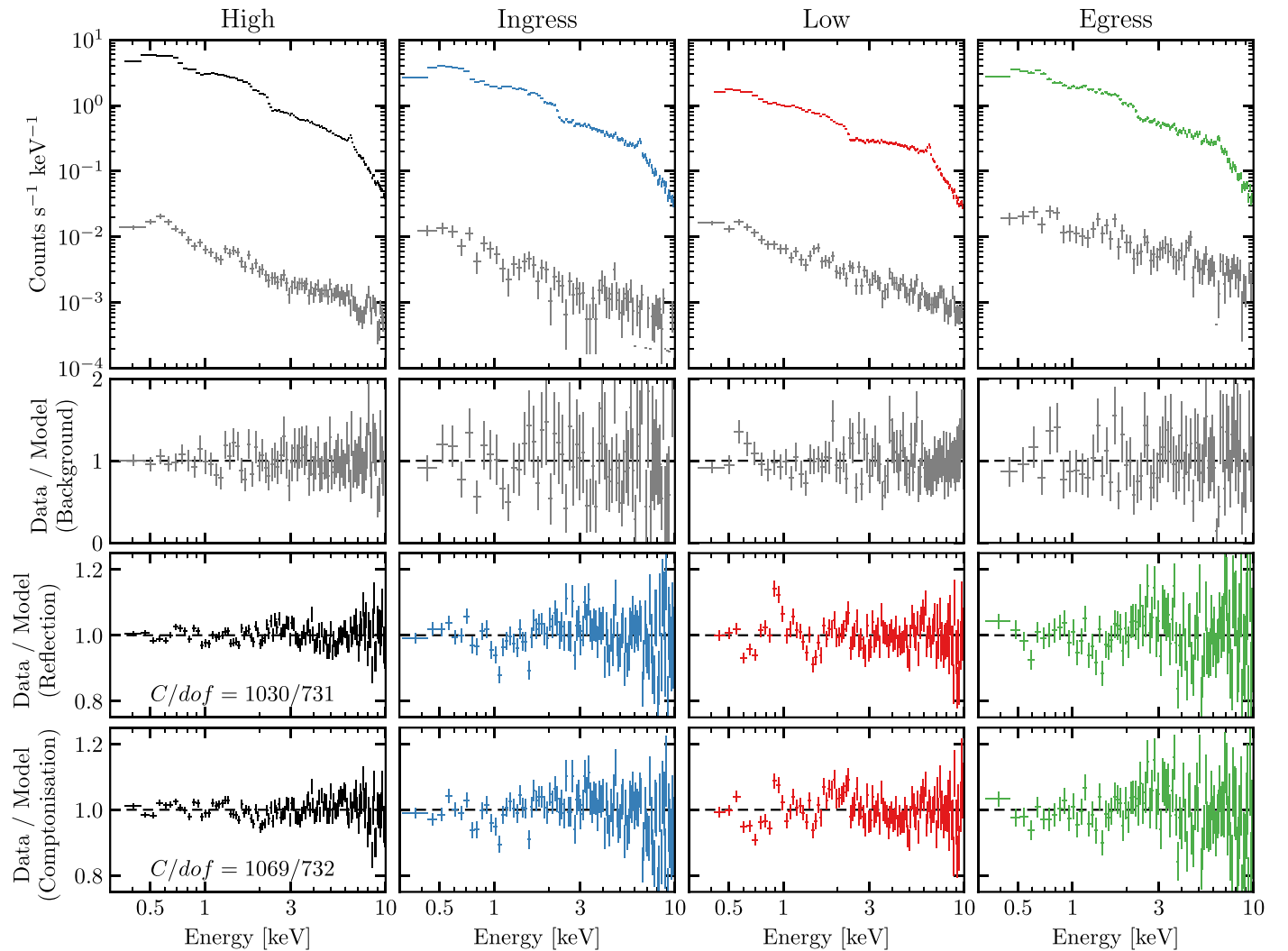
Figure 4. Partial covering models applied to different continuum scenarios. Top row: the source and background pn spectra between 0.3 and 10 keV during each segment (labeled on top). Upper middle row: the residuals from fitting the background data. Lower middle row: the resulting residuals from the ionized blurred reflection model described in the text and in Table 2. Bottom row: the resulting residuals from the soft-Comptonization model described in the text and in Table 2.

spectral and temporal measurements. The depth of the eclipse is energy- dependent (Figure 3), with the low-energy X-rays diminishing to ∼20% of the pre-eclipse brightness and the high-energy X-rays to ∼50%. There is some indication the shape of the eclipse may also differ—at higher energies, the transitions between time points might be smoother than at lower energies. This may be an indication the source size is energy dependent and that the high-energy X-rays are more centrally compact. Such limb-darkening behavior is common in stellar and exoplanet transient curves.

We modeled the 0.3–10 keV spectra from each of the time segments (see Figure 1) simultaneously in a self-consistent manner. We tested different continuum models, which yielded similar results, but for ease of presentation, here we will discuss the results assuming the intrinsic X-ray emission is described by ionized blurred reflection (Ross & Fabian 2005). The continuum emission was also modified by two nonvariable ionized (warm) absorbers and a Gaussian profile at 6.45 ± 0.01 keV. This primary X-ray emission was then obscured by a partial coverer (Holt et al. 1980; Tanaka et al. 2004) that was of constant column density and ionization parameter. The normalization (brightness) and photon index (Γ) of the power-law continuum

were free to vary between segments as is typical in Seyfert galaxies. The reflection fraction ($\mathcal{R}$) was linked indicating the relative fraction of reflected-to-continuum emission remained constant. For the partial coverer, only the covering fraction (C_f) varied between the segments. This fit was acceptable yielding a C-statistic of $C = 1029$ for 731 dof. The partial coverer could be described as having $N_H = (11.1 \pm 1.2) \times 10^{22}\,\mathrm{cm}^{-2}$ and $\xi = (12.3^{+0.9}_{-3.8})\,\mathrm{erg\,s\,cm}^{-1}$. Prior to ingress (Segment 1), the covering fraction was $C_f < 0.01$. During ingress (Segment 2) and egress (Segment 4), $C_f = 0.20 \pm 0.03$ and 0.29 ± 0.04, respectively. The maximum covering fraction ($C_f = 0.56 \pm 0.02$) was returned during the minimum flux (Segment 3).

The mass of the black hole in NGC 6814 is $M_{BH} = 1.09 \times 10^7\,M_\odot$ (Bentz & Katz 2015). Following Turner et al. (2018, Section 6), assuming the obscurer is moving on a Keplerian orbit there is a relationship between the orbit and obscurer properties such that $r^{5/2} = (GM)^{1/2}\frac{L_X \Delta T}{N_H \xi}$. The total duration of the eclipse (from onset of ingress to end of egress) is $\Delta T \approx 70.5$ ks, and the X-ray luminosity prior to eclipse is measured to be $L_X \approx 2 \times 10^{42}\,\mathrm{erg\,s}^{-1}$. This would place the partial coverer at $r \approx 2694\,r_g = 4.34 \times 10^{15}$ cm.

Table 2
The Partial Covering Model Applied to Two Different Continuum Scenarios, Comptonization and Blurred Reflection

Continuum Model	Model Component	Model Parameter	Parameter Value				
			All	High	Ingress	Low	Egress
Comptonization	ztbabs	$N_{\mathrm{H}}/10^{20}$ cm^{-2}	$5.95^{+2.37}_{-1.69}$				
	zxipcf	$N_{\mathrm{H}}/10^{23}$ cm^{-2}	$1.37^{+0.07}_{-0.04}$				
		$\log \xi/\mathrm{erg\,cm^{-2}\,s^{-1}}$	$1.09^{+0.05}_{-0.03}$				
		f_{cov}		$0.16^{+0.04}_{-0.06}$	$0.44^{+0.02}_{-0.04}$	0.80 ± 0.01	$0.52^{+0.03}_{-0.04}$
	nthcomp$_{\mathrm{soft}}$	Γ	$2.10^{+0.36}_{-0.24}$				
		$kT_{\mathrm{e}}/\mathrm{eV}$	113^{+10}_{-3}				
		$kT_{\mathrm{bb}}/\mathrm{eV}$	3				
		Norm$/10^{-3}$ cm^{-2} s^{-1} keV^{-1}	$1.63^{+0.24}_{-0.17}$				
	nthcomp$_{\mathrm{hard}}$	Γ		1.70 ± 0.03	$1.74^{+0.02}_{-0.04}$	1.97 ± 0.04	1.77 ± 0.04
		$kT_{\mathrm{e}}/\mathrm{keV}$	100				
		$kT_{\mathrm{bb}}/\mathrm{eV}$	3				
		Norm$/10^{-3}$ cm^{-2} s^{-1} keV^{-1}		$8.61^{+0.52}_{-0.68}$	$8.58^{+0.70}_{-0.76}$	12.10 ± 1.00	9.48 ± 0.90
	zgauss	E/keV	6.45 ± 0.01				
		σ/eV	141^{+24}_{-19}				
		Norm$/10^{-5}$ ph. cm^{-2} s^{-1}		$6.03^{+0.78}_{-0.60}$	$5.24^{+1.01}_{-1.05}$	$5.09^{+0.72}_{-0.58}$	$6.45^{+1.54}_{-1.66}$
Blurred reflection	zxipcf	$N_{\mathrm{H}}/10^{23}$ cm^{-2}	1.11 ± 0.12				
		$\log \xi/\mathrm{erg\,cm^{-2}\,s^{-1}}$	$1.09^{+0.03}_{-0.16}$				
		f_{cov}		< 0.01	0.20 ± 0.03	0.56 ± 0.02	0.29 ± 0.04
	cflux	$\log F/\mathrm{erg\,cm^{-2}\,s^{-1}}$		$-10.105^{+0.006}_{-0.013}$	$-10.187^{+0.007}_{-0.020}$	$-10.247^{+0.010}_{-0.020}$	$-10.135^{+0.011}_{-0.024}$
	cutoffpl	Γ		$1.99^{+0.02}_{-0.01}$	$1.98^{+0.02}_{-0.03}$	$1.95^{+0.01}_{-0.02}$	$1.93^{+0.02}_{-0.03}$
	const	$\mathcal{R}$	$1.16^{+0.12}_{-0.06}$				
	relxillD	q_{in}	$8.48^{+0.84}_{-0.56}$				
		q_{out}	3				
		$R_{\mathrm{b}}/r_{\mathrm{g}}$	6				
		$a/[\mathrm{cJ/GM^2}]$	0.998				
		$i/°$	66^{+1}_{-4}				
		$\log \xi/\mathrm{erg\,cm^{-2}\,s^{-1}}$	$0.38^{+0.05}_{-0.07}$				
		$\log N_{\mathrm{H}}/\mathrm{cm^{-2}}$	19				
		A_{Fe}	$3.9^{+0.7}_{-0.9}$				
	zgauss	E/keV	6.45 ± 0.01				
		σ/eV	137^{+21}_{-16}				
		Norm$/10^{-5}$ ph. cm^{-2} s^{-1}		$5.41^{+0.79}_{-0.56}$	$5.47^{+0.96}_{-0.86}$	$5.27^{+0.64}_{-0.48}$	$6.77^{+1.39}_{-1.26}$

Note. In XSPEC terminology the Comptonization model is tbabs×ztbabs×WA1×WA2 × (zxipcf × (nthcomp$_{\mathrm{soft}}$ + nthcomp $_{\mathrm{hard}}$) + zgauss) and the blurred reflection model is tbabs×WA1×WA2 × (zxipcf × (cflux×cutoffpl + const×cflux×relxillD)+zgauss). Parameter values without uncertainties are fixed during the fitting.

The electron density of the cloud is $n = L_{\mathrm{X}}/r^2\xi = 8.61^{+0.63}_{-2.65} \times 10^9$ cm^{-3} and from the measured column density we obtain a cloud diameter of approximately $D_{\mathrm{C}} = 1.30^{+0.17}_{-0.42} \times 10^{13}$ cm. The Keplerian velocity of the partial coverer is $V_{\mathrm{K}} = D_{\mathrm{C}}/T_{\mathrm{i}} \approx 10 \times 10^3$ km s^{-1}. The density is comparable to the electron densities estimated for broad-line region (BLR) "clouds" and the velocity and distance are also in agreement with the inner BLR (Netzer 1990; Arav et al. 1998; Bentz et al. 2009).

The narrow Fe Kα emission line in NGC 6814 exhibits a relatively constant flux within uncertainties ($\sim\pm15\%$) in the four different segments implying that it is not affected by the partial coverer. Its equivalent width does change in accordance with continuum flux changes (i.e., largest equivalent width during the low-flux interval). We modeled the line with a Gaussian profile and found it at $E = 6.45 \pm 0.01$ keV and with $\sigma = 136^{+21}_{-16}$ eV. The resulting FWHM $= 320^{+49}_{-38}$ eV, which renders a velocity of

about $(15 \pm 2) \times 10^3$ km s^{-1}. This is compatible with the location of the obscurer so we may have an example of obscuration and re-emission from the same region.

Comparing the duration of ingress to the duration of the low-flux interval provides an estimate of the X-ray source size: $D_{\mathrm{X}} = D_{\mathrm{C}} \times T_{\mathrm{C}}/T_{\mathrm{i}} = 4.20^{+0.54}_{-1.37} \times 10^{13}$ cm $= 26^{+3}_{-8} r_{\mathrm{g}}$. The value is completely consistent with what is normally estimated or assumed for the size of the corona ($\sim 20\, r_{\mathrm{g}}$; Risaliti et al. 2009; Wilkins et al. 2014; Gallo et al. 2015; Wilkins & Gallo 2015; Chartas et al. 2017; Alston et al. 2020).

There are other interesting aspects of the eclipse that are observed. The RGS spectra are generated for the high- and low-flux intervals (Segments 1 and 3, respectively). The high-resolution grating data are well fitted with two warm absorbers that are then applied to the CCD spectra. The difference between the low- and high-flux states can largely be attributed

to a change in normalization, but there are narrow emission features that appear during eclipse. These could be attributed to some scattered emission from the partial coverer or from emission that originates at large distances from the black hole that is only evident when the continuum brightness is suppressed (e.g., in the narrow-line region, starburst region, or torus; Strickland et al. 2004; Longinotti et al. 2019; Buhariwalla et al. 2020).

The detection of rapid eclipsing events in AGN light curves are powerful tools for determining properties of the absorber, the BLR, and of the primary X-ray source. Here, we have reported the discovery of what appears to be a single cloud passing in front of the central engine. The results show that relativistic reflection and partial covering are both natural to the accretion flow and necessary for accurate modeling, not effects that naturally oppose each other. The properties of the absorber imply a BLR origin. The size of the X-ray source is compact and consistent with expectations (Risaliti et al. 2009; Wilkins et al. 2014; Gallo et al. 2015; Wilkins & Gallo 2015; Chartas et al. 2017; Alston et al. 2020). The eclipse shows evidence of energy-dependent effects, which may lead to understanding limb darkening in the corona.

Such events are difficult to detect in the stochastic behavior of AGN light curves, but they are probably not rare. At least some Seyfert 1.5s may offer advantageous viewing angles: high enough to intercept the BLR in a manner that can give eclipses, but low enough to avoid being blocked by a torus. NGC 6814 is probably an excellent target for witnessing such an event. The designation of NGC 6814 as an intermediate Seyfert 1.5 implies we are seeing the AGN at higher inclinations (i.e., more edge-on). Estimates place the BLR in NGC 6814 at an inclination of 60–80° (Rosenblatt et al. 1994), which is consistent with our X-ray measured disk inclination ($67^{+1°}_{-4}$). From our line of sight, the BLR crosses the X-ray source, but through relatively modest obscuration from the torus.

Data in current X-ray archives can be used to search for similar episodes. Long, uninterrupted observations of well-selected sources can be studied more extensively using current missions, and studied even better with future missions.

ORCID iDs

Adam G. Gonzalez ⓘ https://orcid.org/0000-0003-3678-5033

References

Alston, W. N., Fabian, A. C., Kara, E., et al. 2020, NatAs, 4, 597
Arav, N., Barlow, T. A., Laor, A., Sargent, W. L. W., & Blandford, R. D. 1998, MNRAS, 297, 990
Arnaud, K. A. 1996, in ASP Conf. Ser. 101, Astronomical Data Analysis Software and Systems V, ed. G. H. Jacoby & J. Barnes (San Francisco, CA: ASP), 17
Ballantyne, D. R. 2020, MNRAS, 491, 3553
Bentz, M. C., & Katz, S. 2015, PASP, 127, 67
Bentz, M. C., Walsh, J. L., Barth, A. J., et al. 2009, ApJ, 705, 199
Borucki, W. J., Koch, D., Basri, G., et al. 2010, Sci, 327, 977
Buhariwalla, M. Z., Waddell, S. G. H., Gallo, L. C., Grupe, D., & Komossa, S. 2020, ApJ, 901, 118
Cash, W. 1979, ApJ, 228, 939
Chainakun, P., & Young, A. J. 2017, MNRAS, 465, 3965
Chartas, G., Krawczynski, H., Zalesky, L., et al. 2017, ApJ, 837, 26
Czerny, B., Nikołajuk, M., Różańska, A., et al. 2003, A&A, 412, 317
den Herder, J. W., Brinkman, A. C., Kahn, S. M., et al. 2001, A&A, 365, L7
Edelson, R., Turner, T. J., Pounds, K., et al. 2002, ApJ, 568, 610
Evans, P. A., Beardmore, A. P., Page, K. L., et al. 2009, MNRAS, 397, 1177
Fabian, A. C., Zoghbi, A., Ross, R. R., et al. 2009, Natur, 459, 540
Gallo, L. C., Tanaka, Y., Boller, T., et al. 2004, MNRAS, 353, 1064
Gallo, L. C., Wilkins, D. R., Bonson, K., et al. 2015, MNRAS, 446, 633
García, J. A., Fabian, A. C., Kallman, T. R., et al. 2016, MNRAS, 462, 751
Holt, S. S., Mushotzky, R. F., Becker, R. H., et al. 1980, ApJL, 241, L13
Jansen, F., Lumb, D., Altieri, B., et al. 2001, A&A, 365, L1
Jiang, J., Fabian, A. C., Dauser, T., et al. 2019, MNRAS, 489, 3436
Kaastra, J. S., & Bleeker, J. A. M. 2016, A&A, 587, A151
Kaastra, J. S., Mehdipour, M., Behar, E., et al. 2018, A&A, 619, A112
Kaastra, J. S., Mewe, R., & Nieuwenhuijzen, H. 1996, in UV and X-ray Spectroscopy of Astrophysical and Laboratory Plasmas, ed. K. Yamashita & T. Watanabe (Tokyo: Universal Academy Press), 411
Leighly, K., Kunieda, H., Tsusaka, Y., Awaki, H., & Tsuruta, S. 1994, ApJ, 421, 69
Longinotti, A. L., Kriss, G., Krongold, Y., et al. 2019, ApJ, 875, 150
Magdziarz, P., Blaes, O. M., Zdziarski, A. A., Johnson, W. N., & Smith, D. A. 1998, MNRAS, 301, 179
Miller, L., Turner, T. J., Reeves, J. N., et al. 2010, MNRAS, 403, 196
Mizumoto, M., Done, C., Hagino, K., et al. 2018, MNRAS, 478, 971
Mukai, K., Hellier, C., Madejski, G., Patterson, J., & Skillman, D. R. 2003, ApJ, 597, 479
Netzer, H. 1990, in Active Galactic Nuclei, ed. R. D. Blandford et al. (Berlin: Springer), 57
Parker, M. L., Longinotti, A. L., Schartel, N., et al. 2019, MNRAS, 490, 683
Petrucci, P. O., Ursini, F., De Rosa, A., et al. 2018, A&A, 611, A59
Reichert, G. A., Mushotzky, R. F., & Holt, S. S. 1986, ApJ, 303, 87
Risaliti, G., Elvis, M., Fabbiano, G., et al. 2007, ApJL, 659, L111
Risaliti, G., Miniutti, G., Elvis, M., et al. 2009, ApJ, 696, 160
Risaliti, G., Nardini, E., Elvis, M., Brenneman, L., & Salvati, M. 2011, MNRAS, 417, 178
Rosenblatt, E. I., Malkan, M. A., Sargent, W. L. W., & Readhead, A. C. S. 1994, ApJS, 93, 73
Ross, R. R., & Fabian, A. C. 2005, MNRAS, 358, 211
Steenbrugge, K. C., Kaastra, J. S., de Vries, C. P., & Edelson, R. 2003, A&A, 402, 477
Steffen, J. H., Batalha, N. M., Borucki, W. J., et al. 2010, ApJ, 725, 1226
Strickland, D. K., Heckman, T. M., Colbert, E. J. M., Hoopes, C. G., & Weaver, K. A. 2004, ApJS, 151, 193
Strüder, L., Briel, U., Dennerl, K., et al. 2001, A&A, 365, L18
Tanaka, Y., Boller, T., Gallo, L., Keil, R., & Ueda, Y. 2004, PASJ, 56, L9
Tortosa, A., Bianchi, S., Marinucci, A., et al. 2018, MNRAS, 473, 3104
Turner, M. J. L., Abbey, A., Arnaud, M., et al. 2001, A&A, 365, L27
Turner, T. J., Done, C., Mushotzky, R., Madejski, G., & Kunieda, H. 1992, ApJ, 391, 102
Turner, T. J., Miller, L., Reeves, J. N., & Braito, V. 2017, MNRAS, 467, 3924
Turner, T. J., Reeves, J. N., Braito, V., et al. 2018, MNRAS, 481, 2470
Vaughan, S., Edelson, R., Warwick, R. S., & Uttley, P. 2003, MNRAS, 345, 1271
Waddell, S. G. H., & Gallo, L. C. 2020, MNRAS, 498, 5207
Walton, D. J., Zoghbi, A., Cackett, E. M., et al. 2013, ApJL, 777, L23
Wilkins, D. R., & Gallo, L. C. 2015, MNRAS, 449, 129
Wilkins, D. R., Gallo, L. C., Silva, C. V., et al. 2017, MNRAS, 471, 4436
Wilkins, D. R., Kara, E., Fabian, A. C., & Gallo, L. C. 2014, MNRAS, 443, 2746
Willingale, R., Starling, R. L. C., Beardmore, A. P., Tanvir, N. R., & O'Brien, P. T. 2013, MNRAS, 431, 394
Wilms, J., Allen, A., & McCray, R. 2000, ApJ, 542, 914
Zoghbi, A., Miller, J. M., & Cackett, E. 2019, ApJ, 884, 26